

Designing Amphiphilic Conjugated Polyelectrolytes for Self-Assembly into Straight-Chain Rod-like Micelles

K. J. Winchell, Patrick Y. Yee, Yolanda L. Li, Alexander F. Simafranca, Julia Chang, Christian Beren, Xinyu Liu, Diego Garcia Vidales, Robert J. Thompson, Charlene Z. Salamat, Quynh M. Duong, Robert S. Jordan, Benjamin J. Schwartz, William M. Gelbart, Yves Rubin,* and Sarah H. Tolbert*



Cite This: *Macromolecules* 2023, 56, 3160–3170



Read Online

ACCESS |



Metrics & More

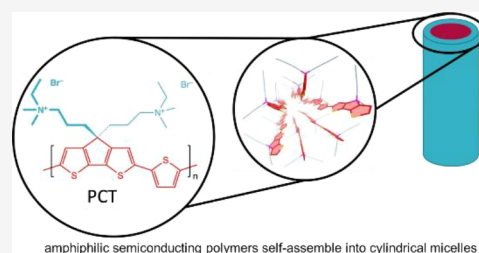


Article Recommendations



Supporting Information

ABSTRACT: Semiconducting polymers are a versatile class of materials that are used in many (opto)electronic applications, including organic photovoltaics. However, they are inherently disordered and suffer from poor conductivities due to bends and kinks in the polymer chains along the conjugated backbone, as well as disorder at grain boundaries. In an effort to reduce polymer disorder, we developed a method to straighten polymer chains by creating amphiphilic conjugated polyelectrolytes (CPEs) that self-assemble in water into worm-like micelles. The present work refines our design rules for self-assembly of CPEs. We present the synthesis and characterization of a straight, micelle-forming polymer, a derivative of poly(cyclopentadithiophene-*alt*-thiophene) (PCT) bearing two ammonium-charged groups per cyclopentadithiophene unit. Solution-phase self-assembly of PCT into micelles is observed by both small-angle X-ray scattering (SAXS) and cryo-electron microscopy (cryo-EM), while detailed SAXS fitting allows for characterization of intra-micellar interactions and inter-micelle aggregation. We find that PCT displays significant chain straightening thanks to the lack of steric hindrance between its alternating cyclopentadithiophene and thiophene subunits, which increases the propensity for the polymer to self-assemble into straight rod-like micelles. This work extends the availability of micelle-forming semiconducting polymers and points to further enhancements that can be made to obtain homogeneous nanostructured polymer assemblies based on cylindrical micelles.



INTRODUCTION

Semiconducting polymers are a useful class of optoelectronic materials thanks to their straightforward solution processability, low cost, and structural tunability. These factors make them a good choice as the active material for a range of organic electronic devices, including photovoltaics, thermoelectrics, light-emitting diodes, and transistors.^{1–4} However, semiconducting polymers suffer from intrinsic disorder that disrupts maximal coplanarity of their conjugated π -system, resulting in decreased conductivity and overall device performance. Because disorder can be so detrimental to polymer device performance, extensive efforts across the field have been targeted at inducing molecular order within semiconducting polymer aggregates.⁵ Semiconducting polymers generally transport charge carriers via two methods: along the π -conjugated backbone of the polymer chain and by chain-to-chain hopping within ordered crystalline π -stacked domains. As such, efforts to increase the order in semiconducting polymers have mostly focused on increasing π -overlap, for example by fusing aromatic rings as in cyclopentadithiophene, and on straightening polymer sidechains to facilitate transport along the polymer chain.^{6,7}

The simplest way to improve transport in conjugated polymers is by increasing the crystallinity in semiconducting

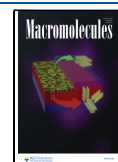
polymer films, as increased crystallinity improves both the π -stacking and the chain straightness.^{8–10} Tuning crystallinity is often achieved by altering film processing conditions, including solvent or substrate choice, deposition speed, and temperature.^{11,12} In addition, polymer crystallinity can be controlled via post-casting treatments, including thermal and solvent annealing.¹³ Another approach is through sidechain engineering.^{5,14–18}

Conjugated polymer order and intrinsic carrier mobility can also be increased by straightening the polymer chains to eliminate inherent trap states where conjugation is broken, and this can additionally increase polymer crystallinity. For example, polymer chains have been straightened by incorporating them into host–guest systems of aligned nanopores,¹⁹ or via mechanical rubbing or solvent shearing,^{20–23} which can increase conductivity by up to three orders of magnitude relative to the unaligned systems.^{24,25} Although post-synthetic

Received: October 6, 2022

Revised: February 12, 2023

Published: April 12, 2023



processing methods like these are promising, they are not likely to be applicable at larger scales because they require special processing that negates many of the attractive aspects of easily processable plastic electronics.

Conjugated polyelectrolytes (CPEs) are polymers that consist of a π -conjugated backbone with charged sidechains, allowing for processing and self-assembly in polar solvents. CPEs are also commonly used as fluorescent sensors in biological systems, thanks to their unique combination of water solubility and easily measured optical properties.^{26–29} In addition, the ion-conducting abilities of some CPEs make them effective interlayer agents in organic electronics such as solar cells and organic electrochemical transistors (OECTs).^{30–32}

In this work, we utilize CPEs to achieve an overall straightening of conjugated polymer chains without post-processing. We introduce intrinsic order and chain straightening by expanding on a previous set of design rules to prepare CPEs that will spontaneously self-assemble in solution into micelles with the polymer chains running along the primary micelle axis.^{33,34} Our design rules take advantage of the unique properties of CPEs to create self-assembled conjugate polymer systems, which may be useful in organic electronic applications.^{33–35} The design rules we proposed to maximize chain straightening were (1) use a hydrophobic conjugated backbone bearing charged sidechains to create amphiphilic behavior; (2) choose an alternating copolymer backbone so that the charged sidechains can all reside on the same side of the polymer backbone when the conjugated π -system is in a near-coplanar conformation; (3) employ dual sidechains that are branched off an sp^3 hybridized carbon within the π -conjugated backbone to hinder π -stacking and create an overall 3-D wedge-shape that promotes self-assembly of the polymer into a cylindrical structure. These rules are represented here by PCT, which is shown in Figure 1.

Using these design rules, we initially synthesized and extensively studied poly(flourene-*alt*-thiophene) (PFT, Figure 1), an alternating copolymer with a hydrophobic conjugated backbone and two positively charged hydrophilic sidechains branching from each fluorene unit. Although water can interact

favorably with the aromatic backbone, the aromatic interactions between chains are much stronger than those with water,³⁶ so the conjugated backbone is not water-soluble. As a result, the effective hydrophobicity of the conjugated backbone and aliphatic sidechains, along with the fact that the charges on the sidechains are designed to all lie on the same side of the backbone, drives self-assembly of this amphiphilic polymer into micelles.^{33–35} The alternating copolymer structure of PFT is key to enabling worm-like micelle formation in aqueous solutions, driven by favorable interactions of water with the charged branched ammonium cations and less favorable interactions between water and the aromatic rings along the polymer chains. Studies of the optical and structural properties of PFT have verified worm-like micelle assembly, along with unusually efficient charge transfer to acceptor molecules that are self-assembled within these micelles.^{33–35}

Herein, a 4th rule expands on the concept of alternating copolymer amphiphilic design: matching connectivity angles between alternating monomer units to straighten the individual polymer chains as much as possible within the self-assembled micelles, as well as minimize steric hindrance to allow monomers to adopt a relatively unhindered coplanar conformation (Figure 1). Micelles are highly dynamic, and fluctuations or partial bond rotations between aromatic units in the copolymer chains should be possible. Despite these dynamic fluctuations, matching connectivity angles and minimizing steric constraints that prevent co-planarization should favor well-ordered rod-like micelle formation, increasing the length of linear regions of the micelle, also known as the persistence length. In PFT, the alternating units have matched bonding angles (Figure 1), but steric compression between the 1,8-hydrogen atoms of fluorene and the 3,4-hydrogen atoms of thiophene units forces the polymer chains out of coplanarity, which gives these chains a much more flexible overall structure (Figure S1). As a result, they would be expected to form less-rigid micelles in an aqueous environment. By exchanging the fluorene with cyclopentadithiophene subunits to obtain poly(cyclopentadithiophene-*alt*-thiophene) (PCT, Figure 1), we gain two advantages over PFT. First, unlike the sterically clashing hydrogen atoms in the neighboring fluorene/thiophene units of PFT, the cyclopentadithiophene and thiophene subunits in PCT have virtually no steric restriction to rotation, increasing the overall probability to maintain a coplanar conformation, and thus an overall straighter polymer backbone (Figure S1). Although the individual aromatic subunits are not frozen in a coplanar conformation, they should be straighter, on average, than in PFT when assembled in a micelle. The straighter backbone of PCT should result in less disordered cylindrical micelles compared to the PFT system. Second, in addition to straightening the polymer chains, the use of cyclopentadithiophene subunits pushes the absorption spectrum well into the red,³⁷ making this polymer much more applicable for use in organic photovoltaics and other visible light absorbing applications.

The expansion of our design rules for straight-chain CPE self-assembly into worm-like micelles in water has been studied using a combination of cryo-EM, solution small-angle X-ray scattering (SAXS), DAMMIN bead modeling, and CRYSOLO simulation of the SAXS scattering data. To aid with the interpretation of $P(r)$ patterns, close-packed bead modeling was employed to simulate patterns for expected particle shapes. We find that low molecular weight PCT forms relatively

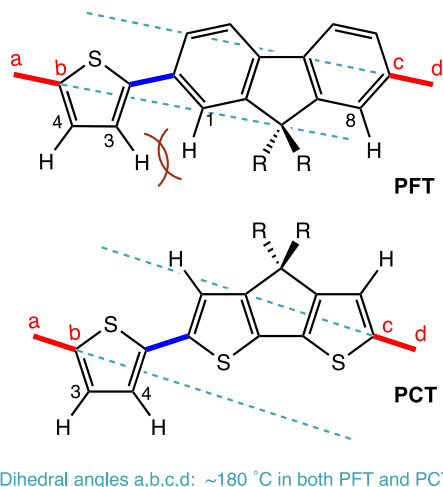


Figure 1. Comparison of the steric mismatch and match between PFT and PCT, showing that the 1,8-hydrogen atoms of fluorene and 3,4-hydrogen atoms of thiophene units force these rings to rotate out of coplanarity in PFT. R = $\text{CH}_2\text{CH}_2\text{CH}_2\text{N}^+\text{Me}_2\text{Et}$ for both polymers.

straight, rod-like micelles at low concentrations, while micelle aggregation occurs at higher concentrations and that high molecular weight PCT produces bent, worm-like micelles. Additionally, PCT shows absorption that is ~150 nm red-shifted from PFT. Moreover, PCT forms well-ordered micelles at low concentrations, while micelle disorder and aggregation increase at higher concentrations. Overall, we demonstrate that our design rules are verified and expanded to allow for the design of different types of amphiphilic micelle-forming polymer chains with a range of different band gaps.

EXPERIMENTAL SECTION

Materials. Chemical reagents were obtained from commercial sources and used without further purification. Unless otherwise noted, all reactions were performed under argon at 25 °C. Silicycle (Siliflash P60) silica gel 60 (240–400 mesh) was used for all column chromatography. Cyclopentadithiophene was purchased from Combi-blocks at 98% purity. Tetrabutylammonium bromide was purchased from TCI America at 99% purity. *N,N*-Dimethylacrylamide was purchased from Sigma Aldrich at 99% purity. *N*-Bromosuccinimide was purchased from TCI at 98% purity. Lithium aluminum hydride was purchased from Sigma Aldrich at 95% purity. 2,5-Bis-(tributylstannyl)thiophene was purchased from Sigma Aldrich at 97% purity. Tetrakis(triphenylphosphine)palladium was purchased from Strem at 99% purity. Ethyl bromide was purchased from Thermo Scientific at 98% purity.

Syntheses. 3,3'-(4*H*-Cyclopenta[2,1-*b*:3,4-*b'*]dithiophene-4,4-diy)bis(*N,N*-dimethylpropanamide) (**1**). Cyclopentadithiophene (1.50 g, 8.40 mmol, 1.0 equiv) was dissolved in toluene (15 mL) along with tetrabutylammonium bromide (250 mg, 0.840 mmol, 0.1 equiv) and *N,N*-dimethylacrylamide (3.33 g, 33.6 mmol, 4.0 equiv) and sparged with argon for 15 min. Separately, a 50 wt % solution of sodium hydroxide (7.5 mL) was sparged under argon. The sodium hydroxide solution was then added dropwise to the reaction mixture and heated at 65 °C overnight. After cooling to 25 °C, the solution was washed with 1 M NaOH and then brine. The organic layer was dried over MgSO₄ and concentrated in vacuo. The residue was triturated with *n*-pentane and the suspension filtered to yield compound **1** as a tan solid (2.66 g, 91%). ¹H NMR (500 MHz, CDCl₃): 7.17 (d, *J* = 4.7 Hz, 2H), 6.94 (d, *J* = 4.7 Hz, 2H), 2.77 (s, 6H), 2.63 (s, 6H), 2.35 (m, 4H), 1.73 (m, 4H) (Figure S2). ¹³C NMR (500 MHz, CDCl₃): 172.0, 153.9, 137.1, 124.8, 112.1, 54.1, 37.1, 35.4, 32.9, 27.5 (Figure S3). HRMS (DART) calculated for C₁₉H₂₄N₂O₂S₂: 377.1352; found: 377.1337.

3,3'-(2,6-Dibromo-4*H*-cyclopenta[2,1-*b*:3,4-*b'*]dithiophene-4,4-diy)bis(*N,N*-dimethylpropanamide) (**2**). Compound **1** (4.00 g, 15 mmol, 1.0 equiv) was dissolved in THF (100 mL) along with *N*-bromosuccinimide (4.29 g, 24.1 mmol, 2.1 equiv). The reaction vessel was covered in aluminum foil and stirred at 25 °C overnight under argon. This mixture was concentrated in vacuo, and the residue was redissolved in chloroform and washed with 10% aqueous sodium thiosulfate, 1 M sodium hydroxide, and then brine. The organic layer was dried over MgSO₄ and evaporated on a Rotavap before purification by chromatography on silica gel using hexanes/CH₂Cl₂/MeOH (1:1:0.1) as an eluent to give compound **2** as a tan solid (4.98 g, 81%). ¹H NMR (500 MHz, CDCl₃): 6.95 (s, 2H), 2.81 (s, 6H), 2.68 (s, 6H), 2.32 (m, 4H), 1.73 (t, 4H) (Figure S4). ¹³C NMR (500 MHz, CDCl₃): 172.5, 155.9, 137.3, 125.4, 121.7, 52.4, 37.0, 35.3, 33.3, 27.8 (Figure S5). HRMS (ESI) calculated for C₁₉H₂₂N₂O₂S₂ [MH⁺]: 532.9568; found: 532.9528.

3,3'-(2,6-Dibromo-4*H*-cyclopenta[2,1-*b*:3,4-*b'*]dithiophene-4,4-diy)bis(*N,N*-dimethylpropan-1-amine) (**3**). Lithium aluminum hydride (874 mg, 23.0 mmol, 3.0 equiv) was dissolved in THF (50 mL) in a flame-dried round-bottom flask and then cooled to 0 °C in an ice bath before concentrated sulfuric acid was added dropwise (2.45 mL, 46.1 mmol, 6.0 equiv) to generate AlH₃ in solution. After stirring for 5 min, a solution of **2** (3.89 g, 7.68 mmol, 1.0 equiv) in THF (77 mL) was added and refluxed overnight under argon. The reaction was quenched with 1 M HCl at 0 °C and then basified with 1 M NaOH.

The precipitate was filtered and washed with THF. The resulting filtrate was washed with brine and dried over MgSO₄ and then evaporated on a rotary evaporator. The product was purified on silica gel with 5% MeOH in CH₂Cl₂ to give 3.12 g of bisamine **3** as a white solid (80%). ¹H NMR (500 MHz, CDCl₃): 6.94 (s, 2H), 2.2–2.1 (m, 16 H), 1.83 (m, 4H), 1.07 (m, 4H) (Figure S6). ¹³C NMR (500 MHz, CDCl₃): 155.3, 136.6, 124.4, 111.5, 59.6, 54.6, 45.4, 35.2, 22.6 (Figure S7). HRMS (ESI) calculated for C₁₉H₂₆N₂O₂S₂ [MH⁺]: 504.9982; found: 504.9826.

Poly{(4,4-bis(3'-(*N,N*-dimethylamino)propyl)cyclopenta[2,1-*b*:3,4-*b'*]dithiophene)-2,6-diyl-alt-(thiophene-2,5-diyl)} (**4**, U-PCT). 2,5-Bis(tributylstannyl)thiophene (4.08 g, 6.16 mmol, 1.0 equiv) and bisamine **3** (3.12 g, 6.16 mmol, 1.0 equiv) were dissolved in THF (175 mL) and sparged for 15 min under argon before tetrakis(triphenylphosphine)palladium (712 mg, 0.616 mmol, 0.1 equiv) was added. The reaction was then refluxed for 3 days under argon. Upon cooling to room temperature, the polymer was precipitated with 700 mL of hexanes and centrifuged in separate aliquots. The supernatant was decanted, and the process was repeated until the supernatant was light purple. The resulting polymer was vacuum dried to yield 1.85 g of purple solid (69%). ¹H NMR (500 MHz, CDCl₃): 7.9–6.5 (br m, 4H), 2.4–1.5 (m, 20H), 1.5–1.0 (br m, 4H) (Figure S8). The molecular weight of **4** (referred to as unquaternized PCT, or U-PCT) was determined by gel permeation chromatography (GPC) (2,2,2-trifluoroethanol). *M_n* = 30,000, *M_w* = 37,000, PDI = 1.2.

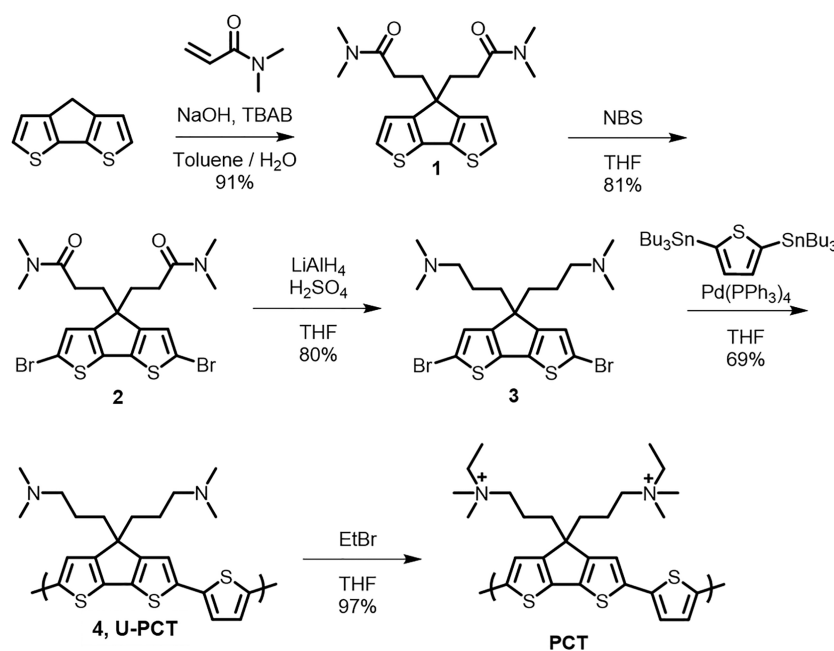
Poly{(4,4-bis(3'-(*N*-ethyl-*N,N*-dimethylamino)propyl)cyclopenta[2,1-*b*:3,4-*b'*]dithiophene)-2,6-diyl-alt-(thiophene-2,5-diyl)} Bromide (PCT). Polymer **4** (100 mg, 1.0 equiv) was dissolved in THF (30 mL) under argon. A very large excess of ethyl bromide (15 mL) was added, and the mixture was refluxed for 4 days. The cooled mixture was evaporated on a rotavapor to yield 146 mg of a purple powder (97%). ¹H NMR (500 MHz, DMSO-*d*₆): 7.6–7.2 (m, 4H), 3.13–3.11 (m, overlapping with the H₂O peak), 3.0–2.8 (m, 12H), 2.51 (s, 8H), 1.9–1.7 (br s, 4H), 1.5–1.3 (br m, 4H), 1.3–1.0 (m, 6H) (Figure S9). Size-selective precipitation was performed by dissolving the polymer in minimal dimethyl sulfoxide (DMSO), followed by the addition of sufficient ethyl acetate to generate a visible precipitate. The mixture was centrifuged at 4000 rpm for 15 min to pellet the precipitated high-molecular-weight (high-MW) polymer fraction, and the supernatant was removed. A second precipitation was performed by another addition of ethyl acetate, yielding a low-MW polymer fraction. Both polymer fractions were washed with ethyl acetate and dried under vacuum overnight.

Characterization. Spectroscopy Measurements. UV–vis absorption spectra were acquired using a Shimadzu UV-3101PC UV–vis–NIR scanning spectrophotometer. Solutions were measured using a quartz cuvette with a 1 cm path length. Solution NMR spectra were obtained on a Bruker AV500 instrument.

Molecular Weight Measurements. Gel permeation chromatography traces were obtained from a JASCO GPC with a UV-4075 UV detector and an RI-4030 refractive index detector. The mobile phase was 2,2,2-trifluoroethanol with 20 mM sodium trifluoroacetate as an additive, operating at a flow rate of 500 μL/min. The equipped columns were two in tandem, 300 mm PSS PFG analytical linear columns with 5 μm particle size. The samples were calibrated to poly(methyl methacrylate) standards manufactured by PSS.

Cryo-Electron Microscopy (Cryo-EM). Cryo-EM grids were prepared using a Vitrobot Mark IV cryo-sample plunger. A total of 2 μL of polymer sample at a concentration of 0.5 mg/mL was deposited onto a glow-discharged Quantifoil holey-carbon grid (SPI Quantifoil R3.5/1). The grid was then blotted dry and rapidly frozen by plunging into a 2:1 mixture of liquid propane to liquid ethane cooled to liquid nitrogen temperature, producing thin films of vitreous ice containing the sample in the holey carbon film. Grids were imaged on an FEI (Hillsboro, OR) Tecnai G2 TF20 EM (Electron Imaging Center for Nanomachines, California Nanosystems Institute, Los Angeles, CA) operating with an accelerating voltage of 200 kV. Images were acquired in transmission mode with a TIETZ F415MP 4k × 4k pixel CCD camera at 50k× magnification with a defocus

Scheme 1. Greatly Improved Synthetic Approach to PCT Making Use of a Double Michael Addition of *N,N*-Dimethylacrylamide onto Cyclopentadithiophene



value of 3–4 μm , and the total beam exposure was maintained between 20 and 40 $\text{e}/\text{\AA}^2$.

Solution SAXS. Solution SAXS was collected at the Stanford Synchrotron Radiation Lightsource using beamline 4-2. The solution samples were dissolved in milli-Q ultrapure water and loaded into a quartz capillary and held at room temperature. The scattering X-rays (12 keV) were collected using a 2D detector at a sample-to-detector distance of 1.7 m. The 2D patterns were radially averaged to obtain the 1D scattering curves. GNOM, DAMMIN, and CRY SOL, packages in the ATSAT software suite developed by the European Molecular Biology Laboratory (EMBL), were utilized to process and fit the SAXS data. The $P(r)$ plots were obtained using the GNOM software from the European Molecular Biology Laboratory.³⁸ The smoothed 1D SAXS data were used for bead modeling, using DAMMIN, Monte Carlo-based modeling software.³⁹ CRY SOL, another feature in the ATSAT software package, was used to simulate and fit atomic model structures to experimental SAXS data.⁴⁰ Parameters for the bead modeling and CRY SOL simulation can be found in the Supporting Information (SI).

J–V Device Fabrication and Measurement. Devices were fabricated on 1.5 cm \times 1.5 cm indium tin oxide (ITO)-coated glass substrates, which were cleaned by sonicating successively in soap water, deionized water, ethanol, dichloromethane, and acetone for 15 min each. Substrates were then plasma cleaned using a PDC-32G set to a low RF level for 5 min. PCT films were spin-cast onto the clean substrates using a VTC-100 spin coater at 2100 rpm for 90 s from a 20 mg/mL aqueous solution of high-MW PCT. U-PCT films were drop-cast from 10 μL of a 10 mg/mL ethanolic solution. The solution layer was allowed to equilibrate with its vapor in a petri dish before the dish was opened slightly to induce drying. Films were completely dried by storing under vacuum overnight. An aluminum layer of 80 nm was deposited at a rate of 0.5 $\text{\AA}/\text{s}$ under vacuum resulting in an electrode surface area of 6.6 mm^2 . The dark current injection was performed using a Keithley 2400 sourcemeter under ambient conditions. The thicknesses of the U-PCT and PCT films were measured using a Dektak 150 profilometer. The measured thicknesses were 111 and 198 nm for U-PCT and PCT, respectively.

Grazing Incidence Wide Angle X-ray Scattering (GIWAXS). GIWAXS data were collected at the Stanford Synchrotron Radiation Lightsource (SSRL) using beamline 11-3. The beam energy was 12.7 keV, and the incidence angle was 0.12 $^\circ$. The sample-to-detector

distance was 250 mm. The sample chamber was filled with helium, and the samples were irradiated for 90 s each. Scattering was collected on an area detector, and the 2D diffraction patterns were radially integrated to produce 1D diffraction patterns shown here using the WAXStools package in Igor Pro.

RESULTS AND DISCUSSION

Figure 1 and Scheme 1 show the structure of amphiphilic PCT, indicating how a straight backbone is achieved by using cyclopentadithiophene and thiophene as the monomeric units; amphiphilicity is conferred by incorporating two hydrophilic ammonium sidechains per cyclopentadithiophene unit branching off the backbone of the polymer. The total synthesis of PCT has been realized as shown in Scheme 1. We found that it was much easier to introduce these sidechains via a double Michael addition of *N,N*-dimethylacrylamide at the sp^3 carbon of the cyclopentadithiophene moiety (Scheme 1), which considerably enhances the yields of the intermediates compared to the more traditional double alkylation approach with $\text{ClCH}_2\text{CH}_2\text{CH}_2\text{NMe}_2$.^{30,31,34} Our attempts to pursue the latter approach resulted in complete loss of the very expensive cyclopentadithiophene starting material. The NMR characterization data for the intermediates and final products can be found in Figures S2–S9. We have also shown that introducing the sidechains via double Michael addition works with fluorene in addition to cyclopentadithiophene (Figures S10–S12). Subsequent bromination of the outer cyclopentadithiophene rings followed by reduction of the *N,N*-dimethylamide in 2 to *N,N*-dimethylamine in 3 using in situ generated AlH_3 yielded the monomeric core (3) of PCT. After copolymerization of 3 with 2,5-bis(tributylstannyl)thiophene, polymer 4, or U-PCT, was quaternized with excess bromoethane to generate the hydrophilic *N,N*-dimethyl-*N*-ethylammonium moieties in PCT. The versatility of this strategy allows for straightforward changes to the core or side chains of these or other linker units and thus allows us to obtain a potential library of amphiphilic polymers.

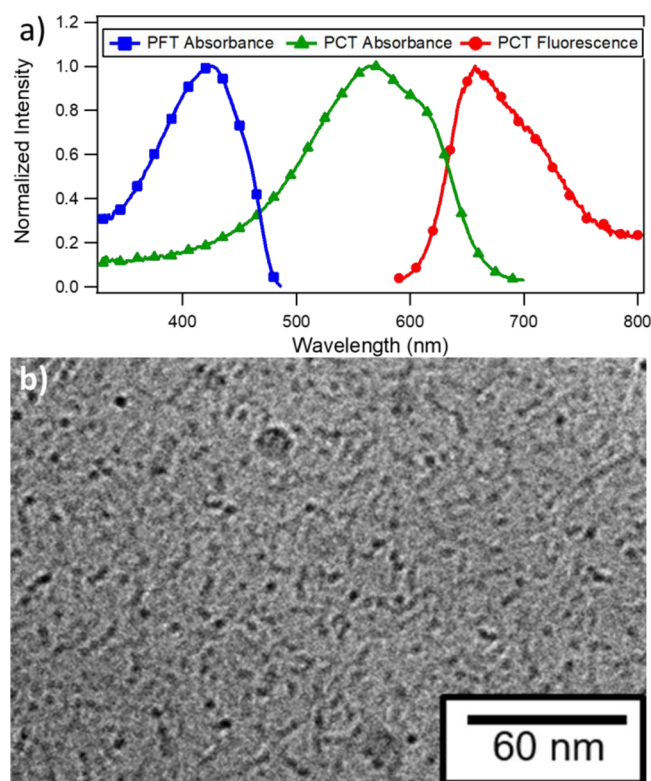


Figure 2. (a) Optical characterization of PCT showing that its lower band gap results in absorption in most of the visible region, compared to PFT which absorbs only in the blue. (b) Cryo-EM micrograph of a frozen PCT solution showing micelle-like structures with an average diameter of 2 nm.

Optical characterization of PCT in aqueous solution is shown in Figure 2a. The absorption spectrum of PCT shows a band gap that is red-shifted by ~ 150 nm compared to the previously studied micelle forming polymer, PFT. The large shift is the result of exchanging higher band-gap fluorene units for lower band-gap cyclopentadithiophene units. As expected, the emission spectrum is also shifted to lower energy and is centered in the red region of the visible spectrum.

These optical spectra demonstrate that the band gap of the CPEs created using our design rules can easily be tuned, with only minor changes in the backbone structure.⁴¹

To investigate the self-assembly of PCT into worm-like micelles, we began with cryo-EM on flash-frozen dilute aqueous solutions of PCT, as seen in Figure 2b. The cryo-EM samples were prepared as described in the Experimental Section, producing thin films of vitreous solution suspended across holey-carbon grids. The resulting image shows many individual micelles overlapping one another, with dark spots indicating points of intersection. Each micelle measures about 2 nm in diameter. Because the electron density contrast between water and PCT is low, the TEM image in Figure 2b is not well resolved. It is nevertheless a real-space image of the self-assembled PCT micelles that form in aqueous solutions.

To complement the cryo-EM images, we used SAXS to provide more quantitative information on the size and shape of self-assembled PCT micelles and aggregates in solution. All samples measured by solution SAXS underwent size-selective precipitation to separate high- and low-molecular weight (MW) polymers prior to dissolution in water, as described in the Experimental Section. The raw SAXS scattering curves in

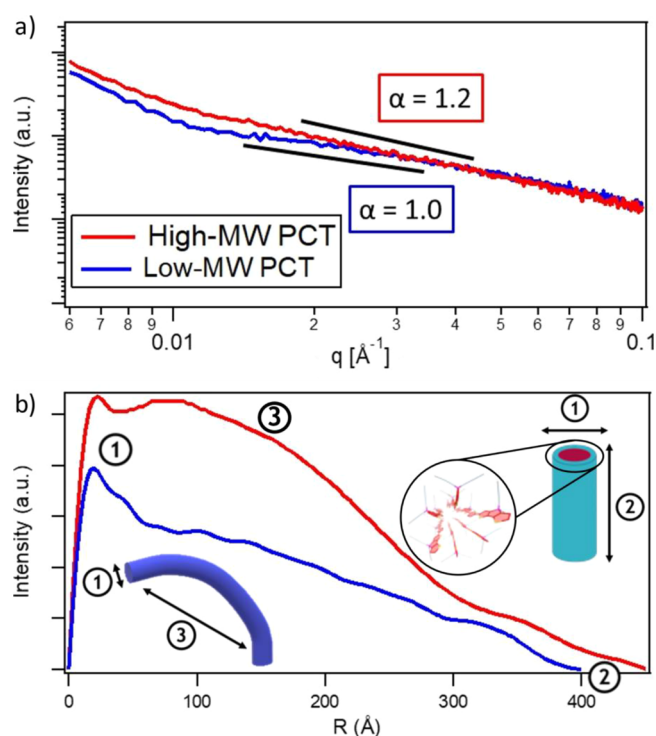


Figure 3. (a) Radially averaged SAXS data with power-law fits, and (b) $P(r)$ transformations of the SAXS data confirming rod-like micelle structures for both high- (red) and low- (blue) MW PCT in water. The right inset in panel (b) and the numbers on the curves show where the micelle diameter (region 1) and length (region 2) are reflected in the data, and the left inset shows how micelle curvature results in correlations across the curve (region 3).

Figure 3a for both high- and low-MW PCT samples (red and blue curves, respectively) are fairly featureless, which is expected for cylindrical micelles in solution.^{35,42,43} The general shape of the solution self-assembly can be determined by fitting to a power law based on the Guinier–Porod model, wherein the power-law slope is indicative of the polymer fractal structure.⁴⁴ In essence, this power law slope is representative of the dimensionality of the average shapes in solution: slopes of 1, 2, and 3 correlate to rods, disks, and spherical structures, respectively. Interactions between molecules, or branching/bending in the case of rods, can result in deviations from a slope of 1.

The power-law slope is properly measured for worm-like micelles in the region given by the Guinier–Porod model. This region roughly lies between the q -values corresponding to the diameter and length of the micelles.⁴⁴ Preliminary estimates for a rod-shape micelle (diameter = 20 Å, length = 400 Å) suggest that the intermediate- q region that follows the power law lies in 0.011 – 0.24 Å⁻¹ (calculations described in the SI). Figure 3a shows that for both the high- and low-MW PCT scattering profiles have slopes near 1 in this region, with the low-MW scattering profile fitting precisely to 1. The higher power-law slope of 1.2 for high-MW PCT may be explained by micellar bending, as shown in the left inset of Figure 3b. For comparison, the power-law slope of low-MW PFT is 1.4 (Figure S13), and it is 1.5 for high-MW PFT.³² This is evidence that the absence of steric compression between the hydrogen atoms of neighboring thiophene and cyclopentadithiophene indeed straightens the polymer chains and results in stiffer micelles.

The 1D scattering data shown in Figure 3a can be further interpreted by indirect Fourier transformations to a pair-distance distribution function, $P(r)$, as seen in Figure 3b. The $P(r)$ function represents the average relative probability of electron density correlations at a given separation distance, r .^{42–44} Simulated $P(r)$ patterns with corresponding $I(q)$ patterns for various ideal shapes are shown in Figure 4. The

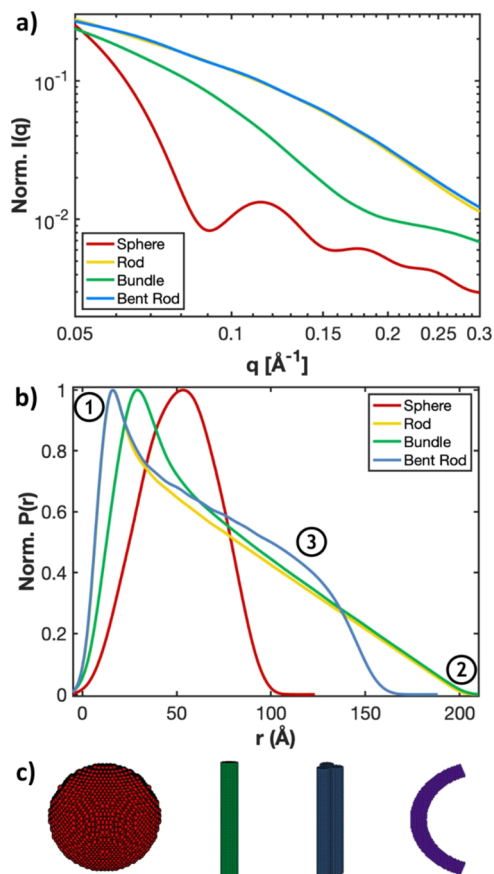


Figure 4. Simulated (a) $I(q)$ and (b) $P(r)$ patterns for possible particle shapes. (c) Close-packed bead models of the possible particle shapes. The selected rod-like shapes represent deviations from an ideal rod by aggregation (bundle) and by deformation (bent rod). It is noteworthy that bending of the rod-like particle produces a distinct difference in the $P(r)$ pattern that is not visually obvious in the $I(q)$ pattern. The computational procedure is described in the SI. Regions 1, 2, and 3 are defined as in Figure 3b.

$P(r)$ functions derived from the SAXS data for low-MW PCT confirm a rod-like micelle, showing a sharp peak correlated with the cylinder diameter (Figure 3b, region 1) followed by a linear decay that terminates at the x axis (region 2) near a value, D_{max} correlated with the long axis length of the micelle. We found that the shape of the linear decay and the intersection with the x axis did not change significantly when iterating the maximum cutoff size (D_{max}), indicating that the fit is robust. For both the high- and low-MW PCT (red and blue curves, respectively), there is a sharp peak near $r = 20$ Å. Particularly in the case of low-MW PCT, $P(r)$ demonstrates a shape nearly identical to that of a straight rod-like particle with a length of 400 Å.

For the high-MW sample, aside from the generally rod-like shape of the $P(r)$ pattern, there is also a broad peak centered at around 150 Å (red curve, regions 3), suggesting that additional

particle correlations are possible with longer chain lengths. The peak in region 3 is likely due to micellar bending, as shown pictorially in the Figure 3b left inset and in Figure 4 for a single radius of curvature ($R_C = 80$ Å). Because the longer polymer chains of high-MW PCT are expected to produce longer micelles, this type of bending fluctuation should become increasingly common in higher molecular weight polymers. Unlike with low-MW PCT, the bent shape of the high-MW PCT micelles disallows correlations along the full length of the micelle, meaning region 2 in this case represents the longest correlations across the bent micelle, instead of the physical length of the micelle. Together, the presence of these intramicellar correlation peaks suggests a more curved shape in high-MW PCT micelles, though the underlying worm-like shape of the micelles is preserved.

To further explore the structure of our amphiphilic polymer assemblies, we also utilized DAMMIN bead modeling, which is a Monte Carlo-based optimization procedure to fit the SAXS data. In the fitting process, the 1D SAXS data were first fit to a smoothly varying function (green curve in Figure 5) so that the

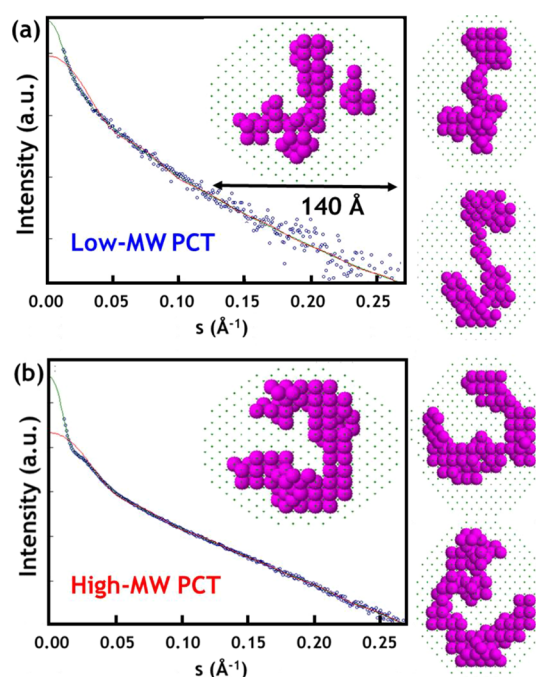


Figure 5. DAMMIN bead model fits and structures for (a) 1 mg/mL high-MW PCT, and (b) 1 mg/mL low-MW PCT. Models for the low-MW PCT show straighter bead segments while those for the high-MW PCT show a significant bending curvature.

Monte-Carlo routine does not try to fit structure to the noise in the data. Beads in a simulation box were then moved using Monte-Carlo methods to create structures whose scattering profiles best matched the fit to the scattering data.³⁹ The fits are usually not unique, so a series of best fit structures are used to define the average best structure in solution. Due to computational limitations, we were not able to use simulations boxes larger than 140 Å, which is smaller than some of the correlation distances shown in Figure 3b. The visible mismatch in the very low- q region is related to this relatively small box size.

DAMMIN bead models for low-MW PCT (Figure 5a) generally show straight, rod-like chains that agree with both the power-law fits and the $P(r)$ data presented in Figure 3. For the

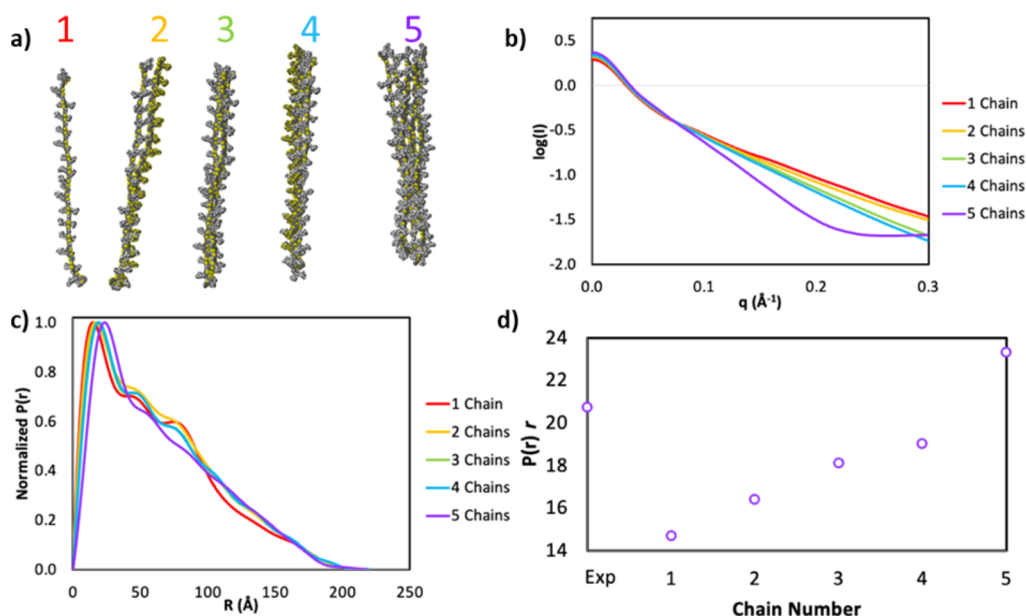


Figure 6. (a) Illustrative atomic structures of PCT micelles with one to five chains generated in Spartan 20. (b) Simulated $I(q)$ data for each of the five structures from part (a) generated using CRY SOL, (c) simulated $P(r)$ data for each of the structures from part (a), generated using CRY SOL. (d) Position of the first correlation peak from the $P(r)$ simulations in part (c).

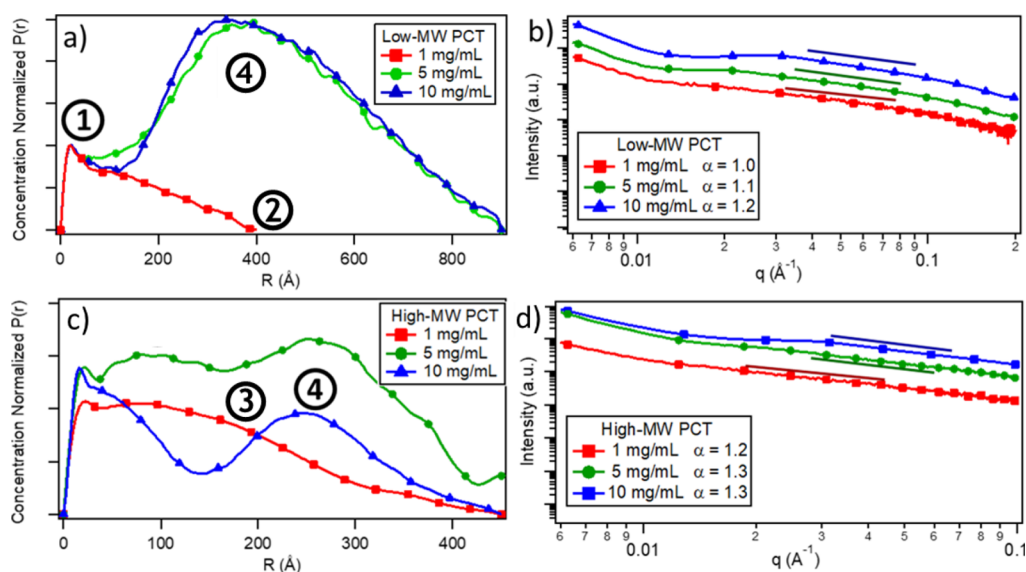


Figure 7. Concentration-dependent $I(q)$ and $P(r)$ patterns for (a, b) low-MW PCT and (c, d) high-MW PCT. $P(r)$ patterns (a, c) were obtained by indirect Fourier transformation of the radially integrated 1D $I(q)$ SAXS patterns (b, d). Power-law slopes (α) are given in the legends for the regions indicated with lines in (b, d). Regions 1–3 in panels (a) and (c) are indicated in relation to the cartoons in Figure 3b, and region 4 represents inter-micellar correlations in aggregated micelles as shown in Figure 7. The position of the region 4 aggregation peak is different for the low and high molecular weight samples, indicating that the nature and details of the aggregated structures vary with micelle length.

high-MW PCT samples, the overall shape of the reconstructions is still rod-like, but now all the cylinders show some curvature (Figure 5b), consistent with the additional intramicellar correlation peak observed in the $P(r)$ pattern. We emphasize that the DAMMIN fits are artificially small, given that the bending-related correlation distances (region 3 of Figure 3b) peak is near ~ 150 \AA and the simulation box is only 140 \AA . Thus, the fits should not be taken as exact structures, but rather as sample configurations that contain features likely found in the real micellar structures. Overall, both the high- and low-MW DAMMIN bead models further demonstrate that PCT forms worm-like micelles in solution. More representative

examples of bead models computed for low- and high-MW PCT are shown in Figures S14 and S15.

To gain more detailed insight into the micellar structure in solution, we utilized the CRY SOL package in the ATSATS software suite to simulate and fit scattering profiles based on model atomic structures.⁴⁰ We built illustrative micellar structures composed of 1–5 chains using the Spartan 20 atomic modeling program and then simulated $I(q)$ and $P(r)$ patterns using CRY SOL (Figure 6). In all cases, the data are qualitatively similar to the measured $I(q)$ and $P(r)$ data. Quantitative comparison allows for differentiation, however. By comparing the position, r , of the diameter-related

correlation peak to the measured peak position (Figure 6d), we estimate that the PCT micelles are composed of 4–6 chains.

To observe how the concentration of polymer in solution affects micelle formation and the types of micellar interactions, solution SAXS was performed on both low- and high-MW PCT at varying concentrations (Figure 7). In non-interacting systems, the scattering profiles do not change shape as the concentration changes, and only the scattering intensity increases with increasing concentration.^{45,46} For interacting systems, however, repulsive or attractive interactions can result in new aggregation-related peaks as concentrations increase. Figure 7a shows concentration-normalized $P(r)$ transformations for the low-MW fraction of PCT. The peak at 20 Å remains the same for all concentrations, indicating that the worm-like shape of the micelles remains unchanged.⁴⁷ However, as the concentration increases, a broad peak appears at ~400 Å, which we define as region 4 likely corresponding to micellar aggregation.

Simulated $P(r)$ patterns for aggregated worm-like micelles (1–3 micelles) are shown in Figure 8. From these patterns, we

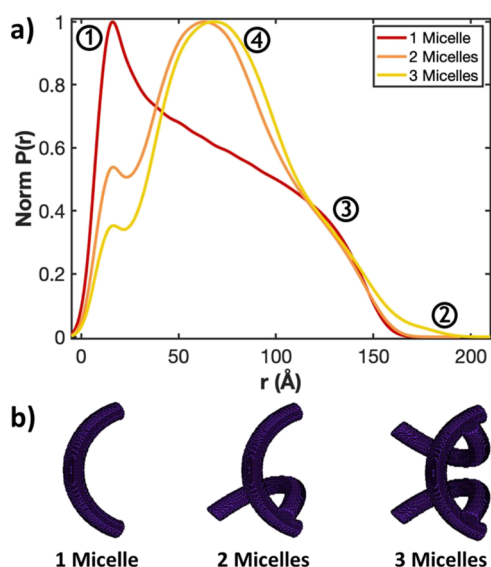


Figure 8. (a) Simulated $P(r)$ patterns for micellar aggregates. (b) Bead models for micelle aggregates composed of 1–3 micelles. The preservation of a diameter-related correlated peak at low r , combined with a spherical correlation peak that dominates the pattern, is characteristic of micellar aggregation.

see that the appearance of a prominent peak resembling the $P(r)$ of a ball-like particle corresponds to correlations between micelles that are close to each other. The shape of the simulated $P(r)$ for a micellar aggregate closely resembles that of the high-concentration low-MW solutions. Because micelles of low-MW PCT are relatively straight due to shorter polymer chain length, the high aspect ratio of the rod-like micelles makes them prone to aggregation. This aggregation also causes an increase in micellar bending due to contact with other micelles, as reflected in the increasing power-law slopes with increased concentrations (from 1.0 at 1 mg/mL to 1.2 at 10 mg/mL) in Figure 7b.

For the high-MW PCT, increasing concentration is again shown to result in the emergence of a new broad peak at a larger distance, but in this case, the peak position is smaller, with a peak at ~250 Å (region 4, Figure 7c). The new peak is

accompanied by a slight increase in the power-law slope (Figure 7d). Although the identity of this peak is not known with certainty, it may also be related to micellar aggregation, with the smaller size resulting because bent micelles are less prone to aggregation. Alternatively, it could be a high-probability nearest-neighbor distance between non-aggregated micelles. Note that this nearest neighbor distance is different from an X-ray structure factor, which requires long-range sample order. Such a nearest-neighbor correlation peak should be absent from the $P(r)$ patterns of low-MW PCT because the low-MW micelles are aggregated at higher concentrations, resulting in very long nearest-neighbor correlations between micellar aggregates that lie outside the measured range. On comparing the $P(r)$ patterns of low- and high-MW PCT, we can conclude that higher-MW PCT permits the formation of bent micellar structures that are less prone to aggregation while lower-MW PCT produces straighter individual micelles that tend to aggregate at higher concentrations.

Given that cryo-EM and solution SAXS confirm that PCT self-assembles into worm-like micelles in aqueous solution, the next question is whether these structures are maintained in PCT films. Although a full film structural study is outside of the scope of this work, some information can be gained from GIWAXS experiments performed on PCT films cast from aqueous solutions. Almost all conjugated polymers show some diffraction due to partial crystallinity induced by π -stacking. Specifically, almost all conjugated polymers show at least two characteristic peaks in their GIWAXS patterns that are correlated with the lamellar distance and a π - π stacking distance. As shown in Figure 9a, this is true for both highly

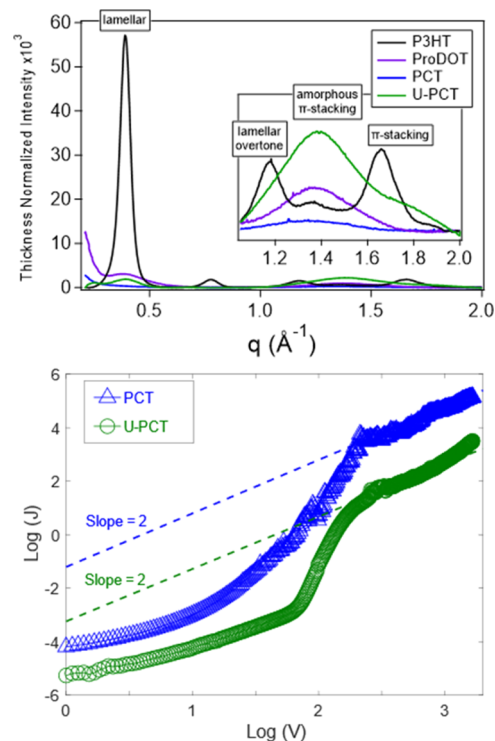


Figure 9. (a) Radially integrated GIWAXS patterns of several films of conjugated polymers. Regardless of crystallinity, conjugated polymers typically show two characteristic peaks (lamellar and π -stacking). However, micelle formation, as shown in the blue curve, disrupts the conjugated polymer's ability to π -stack, resulting in low scattering. (b) SCLC measurements of PCT and U-PCT diodes.

ordered conjugated polymers like poly(3-hexylthiophene-2,5-diyl) (P3HT, black curve) and amorphous conjugated polymers like dihexyl-substituted poly(3,4-propylenedioxythiophene) (ProDOT, purple curve). In agreement with this idea, the non-amphiphilic precursor polymer U-PCT (green curve), which does not have charged sidechains and thus should not form micellar structures, also shows these two peaks (Figure 9a). In contrast, the micelle-forming PCT conjugated polymers show very little scattering (blue curve), suggesting that micelle formation inhibits standard polymer crystallization. Consistent with the hypothesis that micelles are preserved in the solid state is the fact that PCT does show a broad, low intensity peak in the high- q region around 1.4 \AA^{-1} that is usually associated with disorder, partly π -stacked correlations, but the diffraction pattern for PCT shows no hint of a lamellar peak at low q . Although a lack of diffraction is not proof of micelle preservation in the solid state, it is consistent with this hypothesis.

The ability to easily produce nanostructured films of worm-like micelles from solutions by spin-casting is expected to benefit devices that rely on polymer morphology, such as OECTs. To verify that the films produced in this method have electronic properties promising for these applications, the space-charge-limited current (SCLC) method was used to calculate drift mobilities for films of PCT and U-PCT (shown in Figure 9b) deposited on ITO, with evaporated Al used as the top electrode. PCT creates micellar structures in aqueous solutions and likely maintains that structure in the solid state, but U-PCT does not form micelles due to the lack of charged sidechains. Thus, we expect PCT to have a higher drift mobility than U-PCT. As shown in Figure 9b, both films show SCLC behavior with a slope of 2 in a log–log plot at higher voltages, but the turn-on voltage for the PCT film is markedly lower, suggesting improved electrical contacts, perhaps facilitated by the ionic character of the PCT. The drift mobility of the PCT film was calculated to be 40% higher than that of the U-PCT film ($1.4 \times 10^{-7} \text{ cm}^2/\text{V s}$ for PCT, $1.0 \times 10^{-7} \text{ cm}^2/\text{V s}$ for U-PCT), indicating that the worm-like micellar nanostructure of the PCT films increases the drift mobility. This finding opens up the potential for using micelle forming conjugated polymers in thin film device applications.

CONCLUSIONS

With this work, we have demonstrated the utility of our design rules for straightening polymer chains using self-assembling amphiphilic CPEs by exploring the formation of cylindrical micelles in PCT. The band gap of PCT sits in the middle of the visible range, making this polymer well suited for future optoelectronic applications. Solution SAXS characterization of PCT demonstrates that low-MW PCT can form straight rod-like micelles in solution at low concentrations, as suggested by a power-law slope of 1 in the $I(q)$ pattern and corresponding $P(r)$ profile that matches the theoretical shape for a rod-like particle. In high-MW PCT, the micellar structure at low concentrations is worm-like and shows evidence of micellar bending by the presence of intra-micellar correlations in the $P(r)$ pattern in combination with a higher power-law slope in the $I(q)$ pattern. With increasing polymer concentration in solution, the rod-like low-MW PCT micelles begin to aggregate into larger aggregates while the bent high-MW PCT micelles show less aggregation. Regardless of different molecular weights and different concentrations, PCT in solution maintains an underlying worm-like micellar structure,

and films spin-cast from high-MW PCT appear to maintain this structure, resulting in an improved drift mobility compared to the semi-crystalline U-PCT films.

Our design rules for amphiphilic self-assembly of charged conjugated polymers open up exciting potential for further studies in which self-assembling polymers are combined with various excited state electron acceptors to study charge transfer properties, both in solution or in the solid state. Together, our design rules include (1) a hydrophobic core with hydrophilic sidechains, (2) an alternating copolymer in order to ensure that all polar substituents can reside on the same side of the polymer chain after self-assembly, (3) a substituent branching point from an sp^3 carbon created by linking two aromatic rings of a copolymer unit to prevent random polymer aggregation and π -stacking, and lastly, (4) a connecting dihedral angle close to 180° between repeat units of co-monomers and the absence of steric interactions between aromatic units to produce a straighter polymer chain. Due to the high structural tunability within these parameters, many other CPEs can be synthesized using these design rules. This class of water-soluble polymers with inherent order and nearly straight polymer chains may help reduce the many trap states which are typically seen in semiconducting polymers, thereby improving electronic performance in devices.

ASSOCIATED CONTENT

Supporting Information

The Supporting Information is available free of charge at <https://pubs.acs.org/doi/10.1021/acs.macromol.2c02057>.

Synthetic details for all compounds and NMR characterization of products and intermediates; additional SAXS data; and details on DAMMIN bead modeling and addition model fits (PDF)

AUTHOR INFORMATION

Corresponding Authors

Yves Rubin – Department of Chemistry and Biochemistry, University of California Los Angeles, Los Angeles, California 90095-1569, United States; orcid.org/0000-0003-0187-9689; Email: rubin@chem.ucla.edu

Sarah H. Tolbert – Department of Chemistry and Biochemistry, University of California Los Angeles, Los Angeles, California 90095-1569, United States; Department of Materials Science and Engineering, University of California Los Angeles, Los Angeles, California 90095-1595, United States; orcid.org/0000-0001-9969-1582; Email: tolbert@chem.ucla.edu

Authors

K. J. Winchell – Department of Chemistry and Biochemistry, University of California Los Angeles, Los Angeles, California 90095-1569, United States

Patrick Y. Yee – Department of Chemistry and Biochemistry, University of California Los Angeles, Los Angeles, California 90095-1569, United States; orcid.org/0000-0001-7915-1802

Yolanda L. Li – Department of Chemistry and Biochemistry, University of California Los Angeles, Los Angeles, California 90095-1569, United States

Alexander F. Simafranca – Department of Chemistry and Biochemistry, University of California Los Angeles, Los

Angeles, California 90095-1569, United States; orcid.org/0000-0002-5274-4066

Julia Chang – Department of Chemistry and Biochemistry, University of California Los Angeles, Los Angeles, California 90095-1569, United States; orcid.org/0009-0004-0568-3960

Christian Beren – Department of Chemistry and Biochemistry, University of California Los Angeles, Los Angeles, California 90095-1569, United States

Xinyu Liu – Department of Chemistry and Biochemistry, University of California Los Angeles, Los Angeles, California 90095-1569, United States

Diego Garcia Vidales – Department of Chemistry and Biochemistry, University of California Los Angeles, Los Angeles, California 90095-1569, United States

Robert J. Thompson – Department of Chemistry and Biochemistry, University of California Los Angeles, Los Angeles, California 90095-1569, United States

Charlene Z. Salamat – Department of Chemistry and Biochemistry, University of California Los Angeles, Los Angeles, California 90095-1569, United States

Quynh M. Duong – Department of Chemistry and Biochemistry, University of California Los Angeles, Los Angeles, California 90095-1569, United States; orcid.org/0000-0002-8032-101X

Robert S. Jordan – Department of Chemistry and Biochemistry, University of California Los Angeles, Los Angeles, California 90095-1569, United States; orcid.org/0000-0001-9780-6091

Benjamin J. Schwartz – Department of Chemistry and Biochemistry, University of California Los Angeles, Los Angeles, California 90095-1569, United States; orcid.org/0000-0003-3257-9152

William M. Gelbart – Department of Chemistry and Biochemistry, University of California Los Angeles, Los Angeles, California 90095-1569, United States

Complete contact information is available at:
<https://pubs.acs.org/10.1021/acs.macromol.2c02057>

Author Contributions

The manuscript was written through contributions of all authors. All authors have given approval to the final version of the manuscript. K.J.W. and P.Y.Y. contributed equally.

Funding

This work was supported by the National Science Foundation under grant number CHE-2003755.

Notes

The authors declare no competing financial interest.

ACKNOWLEDGMENTS

Use of the Stanford Synchrotron Radiation Lightsource, SLAC National Accelerator Laboratory, is supported by the U.S. Department of Energy, Office of Science, Office of Basic Energy Sciences under Contract No. DE-AC02-76SF00515. The authors acknowledge the use of instruments at the Electron Imaging Center for NanoMachines, supported by NIH (1S10RR23057) and the California NanoSystems Institute (CNSI) at UCLA.

REFERENCES

- (1) Burroughes, J. H.; Bradley, D. D. C.; Brown, A. R.; Marks, R. N.; Mackay, K.; Friend, R. H.; Burns, P. L.; Holmes, A. B. Light-Emitting Diodes Based on Conjugated Polymers. *Nature* **1990**, *347*, 539–541.
- (2) McNeill, C. R.; Greenham, N. C. Conjugated-Polymer Blends for Optoelectronics. *Adv. Mater.* **2009**, *21*, 3840–3850.
- (3) Siringhaus, H.; Bird, M.; Richards, T.; Zhao, N. Charge Transport Physics of Conjugated Polymer Field-Effect Transistors. *Adv. Mater.* **2010**, *22*, 3893–3898.
- (4) Hamid, M.; Abdulameer, D.; Faizul, M.; Sabri, M.; Binti, S.; Said, M.; Haji, M.; Bashir, M.; Bashir, A. A Review on Thermoelectric Renewable Energy: Principle Parameters That Affect Their Performance. *Renewable Sustainable Energy Rev.* **2014**, *30*, 337–355.
- (5) Wu, Y.; Schneider, S.; Walter, C.; Chowdhury, A. H.; Bahrami, B.; Wu, H. C.; Qiao, Q.; Toney, M. F.; Bao, Z. Fine-Tuning Semiconducting Polymer Self-Aggregation and Crystallinity Enables Optimal Morphology and High-Performance Printed All-Polymer Solar Cells. *J. Am. Chem. Soc.* **2020**, *142*, 392–406.
- (6) Mori, H.; Nonobe, H.; Nishihara, Y. Highly Crystalline, Low Band-Gap Semiconducting Polymers Based on Phenanthrothiophene-Benzothiadiazole for Solar Cells and Transistors. *Polym. Chem.* **2016**, *7*, 1549–1558.
- (7) Zheng, Y.; Zhang, S.; Tok, J. B. H.; Bao, Z. Molecular Design of Stretchable Polymer Semiconductors: Current Progress and Future Directions. *J. Am. Chem. Soc.* **2022**, *144*, 4699–4715.
- (8) Hong, C. T.; Yoo, Y.; Kang, Y. H.; Ryu, J.; Cho, S. Y.; Jang, K. S. Effect of Film Thickness and Crystallinity on the Thermoelectric Properties of Doped P3HT Films. *RSC Adv.* **2015**, *5*, 11385–11391.
- (9) Noriega, R.; Rivnay, J.; Vandewal, K.; Koch, F. P.; Stingelin, N.; Smith, P.; Toney, M. F.; Salleo, A. A General Relationship between Disorder, Aggregation and Charge Transport in Conjugated Polymers. *Nat. Mater.* **2013**, *12*, 1038–1044.
- (10) Qian, Z.; Galuska, L. A.; Ma, G.; McNutt, W. W.; Zhang, S.; Mei, J.; Gu, X. Backbone Flexibility on Conjugated Polymer's Crystallization Behavior and Thin Film Mechanical Stability. *J. Polym. Sci.* **2022**, *60*, 548–558.
- (11) Luzio, A.; Criante, L.; D'Innocenzo, V.; Caironi, M. Control of Charge Transport in a Semiconducting Copolymer by Solvent-Induced Long-Range Order. *Sci. Rep.* **2013**, *3*, 3425.
- (12) Panzer, F.; Bässler, H.; Köhler, A. Temperature Induced Order-Disorder Transition in Solutions of Conjugated Polymers Probed by Optical Spectroscopy. *J. Phys. Chem. Lett.* **2017**, *8*, 114–125.
- (13) Aloui, W.; Adhikari, T.; Nunzi, J. M.; Bouazizi, A.; Khirouni, K. Effect of Thermal Annealing on the Electrical Properties of P3HT:PC70BM Nanocomposites. *Mater. Sci. Semicond. Process.* **2015**, *39*, 575–581.
- (14) Bridges, C. R.; Ford, M. J.; Thomas, E. M.; Gomez, C.; Bazan, G. C.; Segalman, R. A. Effects of Side Chain Branch Point on Self Assembly, Structure, and Electronic Properties of High Mobility Semiconducting Polymers. *Macromolecules* **2018**, *51*, 8597–8604.
- (15) Mei, J.; Bao, Z. Side Chain Engineering in Solution-Processable Conjugated Polymers. *Chem. Mater.* **2014**, *26*, 604–615.
- (16) Strzalka, J.; Guo, J.; Chen, L. X.; Xu, T.; Yu, L.; Rolczynski, B. S.; Marks, T. J.; Loser, S.; Lee, B.; Liang, Y.; Szarko, J. M. When Function Follows Form: Effects of Donor Copolymer Side Chains on Film Morphology and BHJ Solar Cell Performance. *Adv. Mater.* **2010**, *22*, 5468–5472.
- (17) Zeman, C. J.; Schanze, K. S. Elucidating the Effects of Solvating Side Chains on the Rigidity and Aggregation Tendencies of Conjugated Polymers with Molecular Dynamics Simulations Using DFT Tight Binding. *J. Phys. Chem. A* **2019**, *123*, 3293–3299.
- (18) Zhang, Q.; Chen, X.; Zhang, B.; Zhang, T.; Lu, W.; Chen, Z.; Liu, Z.; Kim, S. H.; Donovan, B.; Warzoha, R. J.; Gomez, E. D.; Bernholc, J.; Zhang, Q. M. High-Temperature Polymers with Record-High Breakdown Strength Enabled by Rationally Designed Chain-Packing Behavior in Blends. *Matter* **2021**, *4*, 2448–2459.
- (19) Winchell, K. J.; Voss, M. G.; Schwartz, B. J.; Tolbert, S. H. Understanding the Effects of Confinement and Crystallinity on HJ-Coupling in Conjugated Polymers via Alignment and Isolation in an

- Oriented Mesoporous Silica Host. *J. Phys. Chem. C* **2021**, *125*, 23240–23249.
- (20) Ustilova, V.; Biskup, T.; Biniak, L.; Vijayakumar, V.; Brinkmann, M. Control of Chain Alignment and Crystallization Helps Enhance Charge Conductivities and Thermoelectric Power Factors in Sequentially Doped P3HT:F4TCNQ Films. *Macromolecules* **2020**, *53*, 2441–2453.
- (21) Jacobs, I. E.; D'Avino, G.; Lemaire, V.; Lin, Y.; Huang, Y.; Chen, C.; Harrelson, T. F.; Wood, W.; Spalek, L. J.; Mustafa, T.; O'Keefe, C. A.; Ren, X.; Simatos, D.; Tjhe, D.; Statz, M.; Strzalka, J. W.; Lee, J. K.; McCulloch, I.; Fratini, S.; Beljonne, D.; Sirringhaus, H. Structural and Dynamic Disorder, Not Ionic Trapping, Controls Charge Transport in Highly Doped Conducting Polymers. *J. Am. Chem. Soc.* **2022**, *144*, 3005–3019.
- (22) Shaw, L.; Hayoz, P.; Diau, Y.; Reinspach, J. A.; To, J. W. F.; Toney, M. F.; Weitz, R. T.; Bao, Z. Direct Uniaxial Alignment of a Donor-Acceptor Semiconducting Polymer Using Single-Step Solution Shearing. *ACS Appl. Mater. Interfaces* **2016**, *8*, 9285–9296.
- (23) Choudhary, K.; Chen, A. X.; Pitch, G. M.; Runser, R.; Urbina, A.; Dunn, T. J.; Kodur, M.; Kleinschmidt, A. T.; Wang, B. G.; Bunch, J. A.; Fenning, D. P.; Ayzner, A. L.; Lipomi, D. J. Comparison of the Mechanical Properties of a Conjugated Polymer Deposited Using Spin Coating, Interfacial Spreading, Solution Shearing, and Spray Coating. *ACS Appl. Mater. Interfaces* **2021**, *13*, 51436–51446.
- (24) Ghosh, R.; Pochas, C. M.; Spano, F. C. Polaron Delocalization in Conjugated Polymer Films. *J. Phys. Chem. C* **2016**, *120*, 11394–11406.
- (25) Hamidi-Sakr, A.; Biniak, L.; Bantignies, J. L.; Maurin, D.; Herrmann, L.; Leclerc, N.; Lévêque, P.; Vijayakumar, V.; Zimmermann, N.; Brinkmann, M. A Versatile Method to Fabricate Highly In-Plane Aligned Conducting Polymer Films with Anisotropic Charge Transport and Thermoelectric Properties: The Key Role of Alkyl Side Chain Layers on the Doping Mechanism. *Adv. Funct. Mater.* **2017**, *27*, No. 1700173.
- (26) Jiang, Y.; Cui, D.; Fang, Y.; Zhen, X.; Upputuri, P. K.; Pramanik, M.; Ding, D.; Pu, K. Amphiphilic Semiconducting Polymer as Multifunctional Nanocarrier for Fluorescence/Photoacoustic Imaging Guided Chemo-Photothermal Therapy. *Biomaterials* **2017**, *145*, 168–177.
- (27) Pinto, M. R.; Schanze, K. S. Amplified Fluorescence Sensing of Protease Activity with Conjugated Polyelectrolytes. *Proc. Natl. Acad. Sci. U. S. A.* **2004**, *101*, 7505–7510.
- (28) Liu, Y.; Ogawa, K.; Schanze, K. S. Conjugated Polyelectrolytes as Fluorescent Sensors. *J. Photochem. Photobiol., C* **2009**, *10*, 173–190.
- (29) Ambade, A. V.; Sandanaraj, B. S.; Klaikherd, A.; Thayumanavan, S. Fluorescent Polyelectrolytes as Protein Sensors. *Polym. Int.* **2007**, *56*, 474–481.
- (30) Han, M. J.; McBride, M.; Risteen, B.; Zhang, G.; Khau, B. V.; Reichmanis, E.; Yoon, D. K. Highly Oriented and Ordered Water-Soluble Semiconducting Polymers in a DNA Matrix. *Chem. Mater.* **2020**, *32*, 688–696.
- (31) Garcia, A.; Bakus, R. C.; Zalar, P.; Hoven, C. V.; Brzezinski, J. Z.; Nguyen, T. Q. Controlling Ion Motion in Polymer Light-Emitting Diodes Containing Conjugated Polyelectrolyte Electron Injection Layers. *J. Am. Chem. Soc.* **2011**, *133*, 2492–2498.
- (32) Schmode, P.; Ohayon, D.; Reichstein, P. M.; Savva, A.; Inal, S.; Thelakkat, M. High-Performance Organic Electrochemical Transistors Based on Conjugated Polyelectrolyte Copolymers. *Chem. Mater.* **2019**, *31*, 5286–5295.
- (33) Huber, R. C.; Ferreira, A. S.; Aguirre, J. C.; Kilbride, D.; Toso, D. B.; Mayoral, K.; Zhou, Z. H.; Kopidakis, N.; Rubin, Y.; Schwartz, B. J.; Mason, T. G.; Tolbert, S. H. Structure and Conductivity of Semiconducting Polymer Hydrogels. *J. Phys. Chem. B* **2016**, *120*, 6215–6224.
- (34) Huber, R. C.; Ferreira, A. S.; Thompson, R.; Kilbride, D.; Knutson, N. S.; Devi, L. S.; Toso, D. B.; Challa, J. R.; Zhou, Z. H.; Rubin, Y.; Schwartz, B. J.; Tolbert, S. H. Long-Lived Photoinduced Polaron Formation in Conjugated Polyelectrolyte-Fullerene Assemblies. *Science* **1979**, *348*, 1340–1343.
- (35) Clark, A. P.-Z.; Shi, C.; Ng, B. C.; Wilking, J. N.; Ayzner, A. L.; Stieg, A. Z.; Schwartz, B. J.; Mason, T. G.; Rubin, Y.; Tolbert, S. H. Self-Assembling Semiconducting Polymers—Rods and Gels from Electronic Materials. *ACS Nano* **2013**, *7*, 962–977.
- (36) Makhatadze, G. I.; Privalov, P. L. Energetics of Interactions of Aromatic Hydrocarbons with water. *Biophys. Chem.* **1994**, *50*, 285–291.
- (37) Willot, P.; Govaerts, S.; Koeckelberghs, G. The Controlled Polymerization of Poly(Cyclopentadithiophene)s and Their All-Conjugated Block Copolymers. *Macromolecules* **2013**, *46*, 8888–8895.
- (38) Svergun, D. I. Determination of the Regularization Parameter in Indirect-Transform Methods Using Perceptual Criteria. *J. Appl. Crystallogr.* **1992**, *25*, 495–503.
- (39) Svergun, D. I. Restoring Low Resolution Structure of Biological Macromolecules from Solution Scattering Using Simulated Annealing. *Biophys. J.* **1999**, *76*, 2879–2886.
- (40) Svergun, D.; Barberato, C.; Koch, M. H. CRYSOLE - A Program to Evaluate X-Ray Solution Scattering of Biological Macromolecules from Atomic Coordinates. *J. Appl. Crystallogr.* **1995**, *28*, 768–773.
- (41) Wan, Y.; Ramirez, F.; Zhang, X.; Nguyen, T. Q.; Bazan, G. C.; Lu, G. Data Driven Discovery of Conjugated Polyelectrolytes for Optoelectronic and Photocatalytic Applications. *npj Comput. Mater.* **2021**, *7*, 69.
- (42) Svergun, D. I.; Koch, M. H. J. Small-Angle Scattering Studies of Biological Macromolecules in Solution. *Rep. Prog. Phys.* **2003**, *66*, 1735.
- (43) Putnam, D. K.; Lowe, E. W.; Meiler, J. Reconstruction of Saxes Profiles From Protein Structures. *Comput. Struct. Biotechnol. J.* **2013**, *8*, No. e201308006.
- (44) Hammouda, B. A New Guinier-Porod Model. *J. Appl. Crystallogr.* **2010**, *43*, 716–719.
- (45) Hirai, M.; Arai, S.; Iwase, H. Concentration Dependence of Thermal Structural Transition of Hen Egg-White Lysozyme under Constant Heating Rate Studied by Time-Resolved SAXS. *Thermochim. Acta* **2000**, *344*, 95–102.
- (46) Chen, G.; Yu, W.; Singh, D.; Cookson, D.; Routbort, J. Application of SAXS to the Study of Particle-Size-Dependent Thermal Conductivity in Silica Nanofluids. *J. Nanopart. Res.* **2008**, *10*, 1109–1114.
- (47) Yu, D.; Huang, F.; Xu, H. Determination of Critical Concentrations by Synchronous Fluorescence Spectrometry. *Anal. Methods* **2012**, *4*, 47–49.